

Article

Iron-Modified Titanate Nanorods for Oxidation of Aqueous Ammonia Using Combined Treatment with Ozone and Solar Light Irradiation

Silviu Preda ¹, Polona Umek ², Maria Zaharescu ¹, Crina Anastasescu ^{1,*}, Simona Viorica Petrescu ¹, Cătălina Gîfu ³, Diana-Ioana Eftemie ¹, Razvan State ¹, Florica Papa ^{1,*} and Ioan Balint ^{1,*}

¹ “Ilie Murgulescu” Institute of Physical-Chemistry of the Romanian Academy, 202 Splaiul Independentei, 060021 Bucharest, Romania; predas@icf.ro (S.P.); mzaharescu@icf.ro (M.Z.); simon_pet@yahoo.com (S.V.P.); deftemie@yahoo.com (D.-I.E.); rstate@icf.ro (R.S.)

² Jožef Stefan Institute, Jamova Cesta 39, 1000 Ljubljana, Slovenia; polona.umek@ijs.si

³ National Research and Development Institute for Chemistry and Petrochemistry, 060021 Bucharest, Romania; gifu_ioanacatalina@yahoo.com

* Correspondence: canastasescu@icf.ro (C.A.); frusu@icf.ro (F.P.); ibalint@icf.ro (I.B.); Tel.: +4-021-318-85-95 (I.B.)

Abstract: Sodium titanate nanorods were synthesized by a hydrothermal method and subsequently modified with an iron precursor. For comparison, Fe₂O₃ nanocubes were also obtained through a similar hydrothermal treatment. Pristine, Fe-modified nanorods and Fe₂O₃ nanocubes were suspended in diluted ammonia solutions (20 ppm) and exposed to ozone and simulated light irradiation. Ammonia abatement, together with the resulting nitrogen-containing products (NO₃⁻), was monitored by ion chromatography measurements. The generation of reactive oxygen species (·OH and O₂⁻) in the investigated materials and their photoelectrochemical behaviour were also investigated. Morphological and structural characterizations (SEM, XRD, XRF, UV-Vis, H₂-TPR, NH₃-TPD, PL, PZC) of the studied catalysts were correlated with their activity for ammonia degradation with ozone- and photo-assisted oxidation. An increase in ammonia conversion and a decreasing amount of NO₃⁻ were achieved by combining the above-mentioned processes.

Keywords: titanate nanorods; Fe-modified titanate; Fe₂O₃ nanocubes; ammonia catalytic ozonation assisted by solar light



Citation: Preda, S.; Umek, P.; Zaharescu, M.; Anastasescu, C.; Petrescu, S.V.; Gifu, C.; Eftemie, D.-I.; State, R.; Papa, F.; Balint, I. Iron-Modified Titanate Nanorods for Oxidation of Aqueous Ammonia Using Combined Treatment with Ozone and Solar Light Irradiation. *Catalysts* **2022**, *12*, 666. <https://doi.org/10.3390/catal12060666>

Academic Editor: Fernando J. Beltrán Novillo

Received: 1 June 2022
Accepted: 15 June 2022
Published: 17 June 2022

Publisher's Note: MDPI stays neutral with regard to jurisdictional claims in published maps and institutional affiliations.



Copyright: © 2022 by the authors. Licensee MDPI, Basel, Switzerland. This article is an open access article distributed under the terms and conditions of the Creative Commons Attribution (CC BY) license (<https://creativecommons.org/licenses/by/4.0/>).

1. Introduction

The decontamination of waste waters, including the removal of nitrogen-containing pollutants (NH₃), is mandatory in order to sustain the increased global demand of drinking water since natural resources are limited. Therefore, biological water treatments, in addition to advanced catalytic oxidation processes (AOPs) are pathways that are nowadays largely explored by research studies and already validated depollution technologies [1]. High-performance water treatment processes with a view to removing ammonia play a beneficial role in the environment because they contribute to reducing water acidification and eutrophication, contributing to the sustainable use of water resources. In the last decade, many ammonia removal processes have been studied: biological treatment [2], bio filtration treatment [3], air/steam stripping [4] break-point chlorination [5], chemical precipitation [6], ion exchange [7], photo and catalytic ozone oxidation [8,9].

Catalytic ozonation is an advanced oxidation process and has become greatly significant in recent years. During the ozonation process, catalysts favour the decomposition of O₃, generating reactive oxygen species [10]. Many studies [8] indicated the efficient removal of NH₄⁺ by oxidation with ozone using oxide-based catalytic systems of transition metals MO_x (M = Co, Ni, Mn, Sn, Cu, Mg and Al). MgO has a high catalytic activity but low selectivity to N₂ gas, while Co₃O₄ has good selectivity to N₂ gas but a lower activity.

A promising, effective catalyst for NH_4^+ removal, which is selective to nitrogen gas, was reported by Chen et al. [11] using a $\text{MgO}/\text{Co}_3\text{O}_4$ (molar ratio 2:8) composite catalyst. Noble metals supported on metal oxides are also widely investigated and used for aqueous ammonia oxidation into safe gaseous compounds [12–15].

Clearly, many efforts have been made to sustain the implementation of depollution technologies that generate non harmful degradation end-products, but recently, many of these efforts also focused on the usage of green and regenerable energies, such as solar light. For instance, an increased number of photocatalysts were developed and tested in order to achieve the selective degradation of aqueous NH_3 into N_2 under UV and solar light irradiation [16–18]. Most of these are materials based on TiO_2 , displaying a large scale of morphologies and modifiers.

Since titanates with a 1D morphology were extensively and successfully investigated, both for their electronic and optical properties [19–23] it is reasonable to assume that ammonia degradation on these materials can bring significant advancements for environmental preservation. In order to favour the ammonia photodegradation under solar light irradiation, pristine titanate nanorods were modified with iron for the improvement of light absorption and separation of photogenerated charges. These were also compared with bare Fe_2O_3 . Additionally, iron-based compounds are largely used for water depollution processes because they are non-toxic and cheap.

The aim of this work was to optimize the aqueous ammonia oxidation process in order to obtain a high ammonia conversion but also increase selectivity to gaseous nitrogen-containing products. This was successfully achieved by combining the ozone oxidation of aqueous ammonia with its photodegradative abatement under solar irradiation.

2. Results

2.1. Catalysts Synthesis

Sodium titanate nanorods were prepared starting from commercial TiO_2 (anatase). Then, 8 g of TiO_2 was homogenized for 30 min at 3000 rpm in 80 mL 10 M NaOH aqueous solution. The mixture was ultrasonicated for 40 min, and then a definite amount (18 mL) was transferred to the PTFE-lined pressure vessels (Parr Instruments, Moline, IL, USA), with a filling degree of 80%. The pressure vessel was kept at 175 °C for 72 h. The as-obtained mixture was dispersed in distilled water, ultrasonicated for 5 min, filtered to remove excess solution, then dried overnight at 100 °C.

The as-prepared nanorods (denoted TiR) were washed several times using ultrapure water slightly acidified with HCl (pH 6) and further modified with Fe, according to the following procedure: 0.1 g of titanate nanorods were suspended in 3×10^{-2} M $\text{FeCl}_3 \cdot 6\text{H}_2\text{O}$ solution and gently shaken for 24 h. The filtered powder was subjected to hydrothermal treatment in 1 M NaOH solution at 160 °C for 3 h. The sample is denoted as FeTiR.

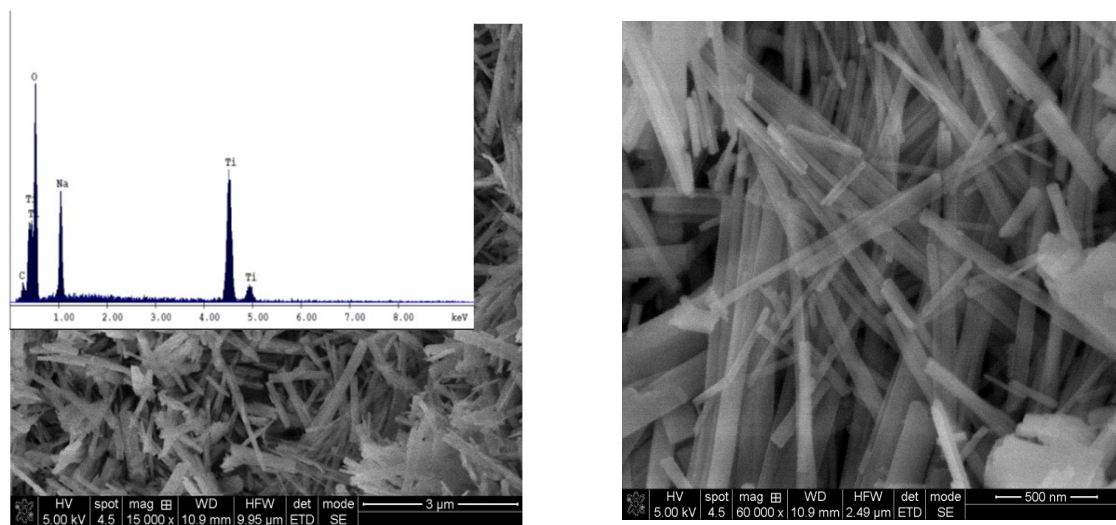
Fe_2O_3 nanocube synthesis follows the above-mentioned hydrothermal procedure, starting from 0.25 g $\text{FeCl}_3 \cdot 6\text{H}_2\text{O}$ and filtering, washing and drying at 80 °C. The sample is denoted as Fe_2O_3 .

2.2. Catalysts Characterisation

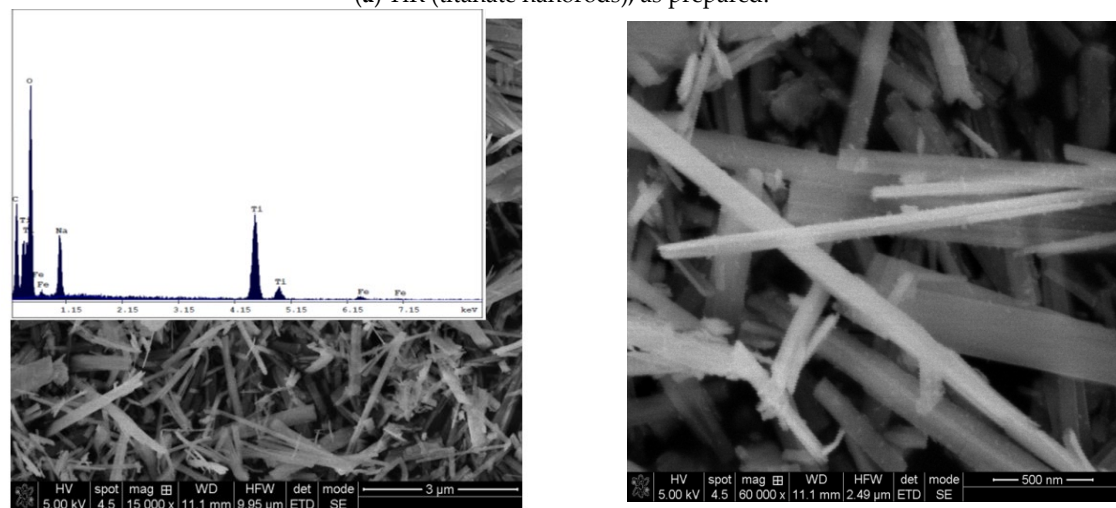
2.2.1. Scanning Electron Microscopy (SEM)

In order to identify the morphological properties of the materials of interest, SEM images were recorded in addition to EDAX analysis.

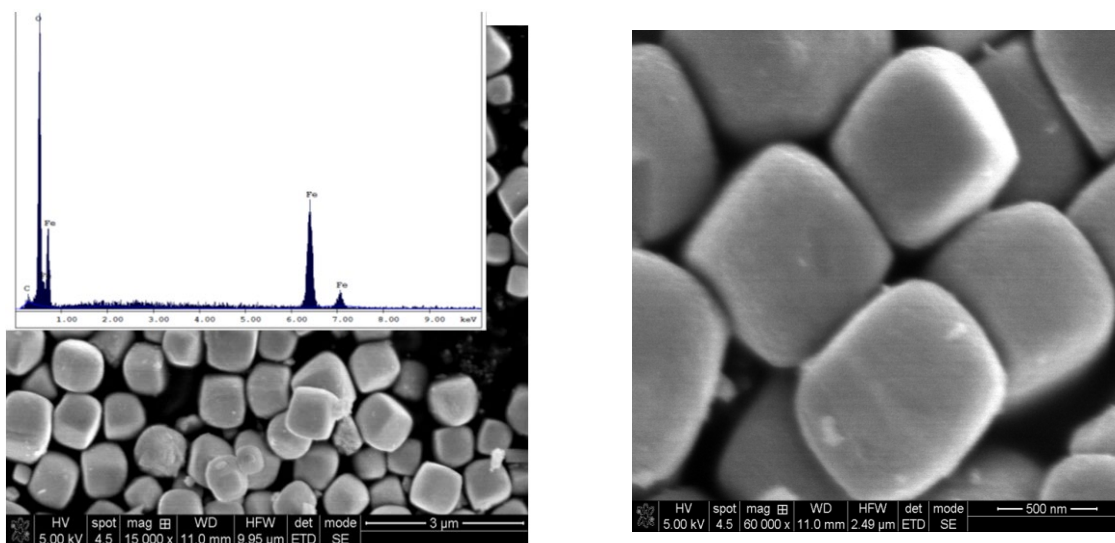
Figure 1a,b reveals a morphological similarity between the as-prepared sodium titanate nanorods and Fe-modified nanorods, their lengths ranging from tens of nanometers to micrometers. A slight loss of transparency, together with an incipient surface roughness, could be perceived in the FeTiR sample, relative to the as-prepared TiR sample. Additionally, EDAX spectra confirmed the presence of iron in the modified nanorods (1.84 wt%) and a smaller sodium amount (7.14 wt%) than for pure nanorods (12.27 wt%).



(a) TiR (titanate nanorods), as prepared.



(b) FeTiR (Fe-modified titanate nanorods).



(c) Fe₂O₃, as prepared.

Figure 1. SEM images and EDAX spectra: (a) TiR as prepared, (b) FeTiR, (c) Fe₂O₃ nanocubes.

Figure 1c shows well-defined Fe_2O_3 nanocubes with a narrow size distribution around 700–800 nm and smooth surfaces. Ma et al. [24] reported the obtaining of Fe_2O_3 microcubes and small nanoparticles depending on the hydrothermal treatment parameters.

2.2.2. X-ray Diffraction (XRD) and X-ray Fluorescence (XRF)

The identification of crystalline phases and elemental characterization was performed in order to explain the catalytic performance of the target materials in the investigated media.

The XRD pattern of the sample TiR, presented in Figure 2a (upper-side), presents typical reflections, which indicates the formation of sodium titanate with nanorods morphology, as also noticed by other groups [25,26]. The phase composition of the sodium titanate nanorods was identified as $\text{NaTi}_3\text{O}_6(\text{OH})\cdot 2\text{H}_2\text{O}$, according to PDF file no. 00-210-4964. The crystal structure of $\text{NaTi}_3\text{O}_6(\text{OH})\cdot 2\text{H}_2\text{O}$ was described as a layered structure, similar to $\text{Na}_2\text{Ti}_3\text{O}_7$, belonging to monoclinic space group $C2/m$. The water molecules of crystallization rendered the structure more open, which is essential for cation-exchange behaviour [25]. The XRF measurement detected the Na/Ti weight ratio of 15/85. The deviation against theoretical ratio was a consequence of the thorough washing procedure after hydrothermal synthesis was completed and the vulnerability of this structure to cation-exchange behaviour.

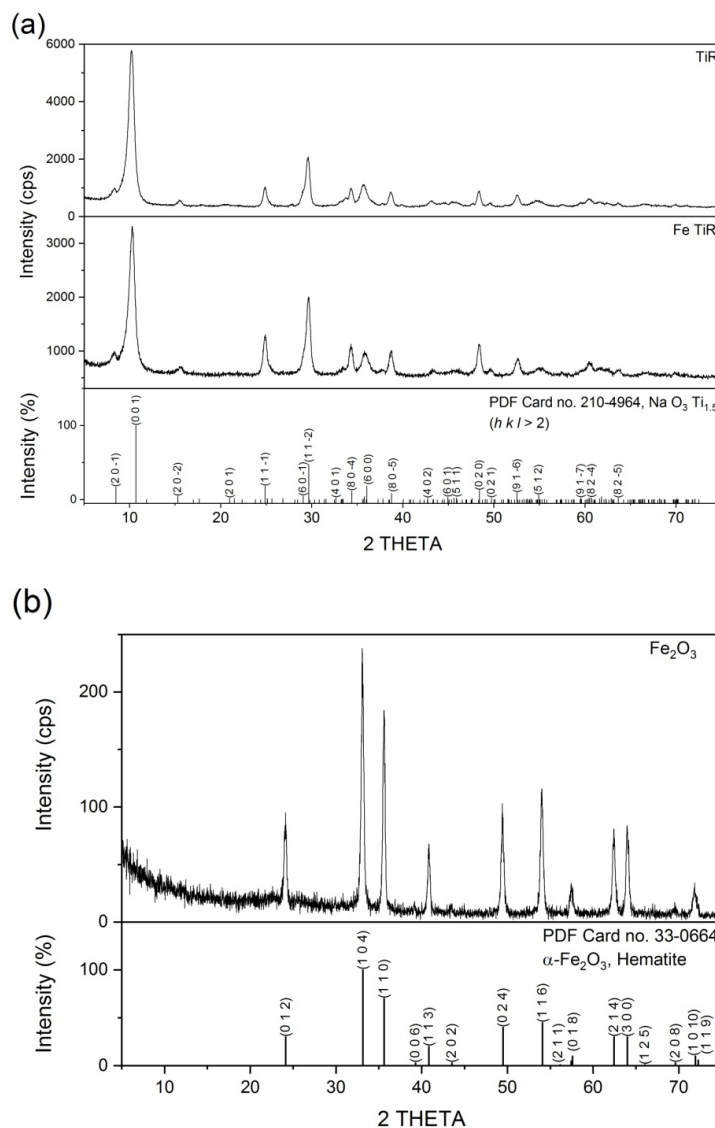


Figure 2. XRD pattern of (a) titanate nanorods: pristine TiR and FeTiR (b) Fe_2O_3 .

Figure 2b (bottom side) presents the sample FeTiR, which contains sodium titanate nanorods submitted for the cation-exchange procedure. Sodium was partially exchanged by iron, as the XRF measurements detected. The weight ratio Fe/Na/Ti was 6/10/84. The percentage of Fe relative to the overall composition, measured by XRF, was 2.9611 mass %. These results are in agreement with the EDAX elemental analysis. Besides the sodium titanate nanorods, no iron-based compounds were detected by XRD. Accordingly, the reasonable assumptions are: the amorphous phase of iron compounds located on the nanorod surface, a partial replacement of sodium by iron cations during the ion-exchange procedure (supported by the XRF results). Furthermore, a shifting of the (001) reflection to smaller 2θ , (for TiR relative to FeTiR sample, respectively, to a larger interlayer spacing (d-value) supports the ion-exchange approach (including sodium–proton exchange).

The XRD pattern of the sample Fe_2O_3 is presented in Figure 2b. Single-phase $\alpha\text{-Fe}_2\text{O}_3$ (hematite) was identified in the sample, according to PDF file no. 00-033-0664. Even single-phase hematite crystallizes, a ~5% amorphous phase can still be detected.

The structure parameters of the three samples are listed in Table 1.

Table 1. The structure parameters.

Sample	(001) Crystal Plane			Unit Cell Parameters				
	2θ ($^\circ$)	d-Value (\AA)	a (\AA)	b (\AA)	c (\AA)	α ($^\circ$)	β ($^\circ$)	γ ($^\circ$)
TiR	10.195(4)	8.670(4)	21.461(10)	3.757(7)	12.113(7)	90	135.59(2)	90
FeTiR	10.291(5)	8.589(4)	21.497(9)	3.7305(16)	12.051(6)	90	135.592(18)	90
Fe_2O_3	-	-	5.038(2)	5.038(2)	13.780(6)	90	90	120

2.2.3. UV–Vis Spectroscopy

The optical properties of the materials were revealed by the recorded diffuse reflectance (DR) spectra, the light absorption characteristics of the catalysts being correlated with their photoactivity.

Figure 3a illustrates a maximum absorption peak located at 260 nm, smaller for TiR and much higher for Fe-modified TiR sample. By enlarging the representation for TiR sample in Figure 3b, a small peak centred at 350 nm can be observed. This appears to be shifted to 390 nm and increased for the Fe-modified nanorods, which unlike the unmodified nanorods, also have a strong absorption in the visible range.

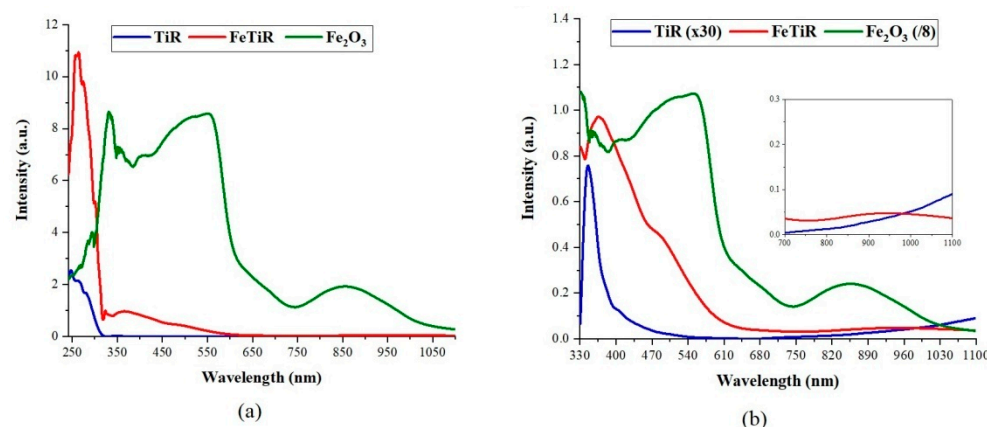


Figure 3. Comparative UV–Vis spectra are as follows: (a) Absorbance of TiR, FeTiR and Fe_2O_3 registered in 250–1100 nm range. (b) Absorbance of TiR (multiplied 30 times), FeTiR and Fe_2O_3 (decreased 8 times) recorded in 330–1100 nm range.

On the other hand, Fe_2O_3 emphasizes a broad light absorption, spanning on the whole spectral range. In the 750–1100 nm domain a broad absorption band can be observed, a similar but discrete shape is perceived in the inset of Figure 3b for the FeTiR sample.

In conclusion, Figure 3a,b clearly shows the improvement of light absorption in the visible range for Fe TiR nanorods relative to pristine TiRs.

2.2.4. Photoluminescence Measurements

Generally, photoluminescence measurements carried out using semiconductors are meant to act as photocatalysts that assess the photogenerated electron–hole pairs recombination and high PL signal, which indicates a reduced photocatalytic activity [27]. By modifying the photocatalyst and its encountering media, different photoluminescence signals can be obtained.

For the TiR and FeTiR samples, Figure 4 shows the same PL emission maxima ($\lambda_{em} = 357$ and 425 nm), which slightly decrease for the Fe-modified nanorods in diluted ammonia solution. This indicates a beneficial photo-mediated interaction between the catalyst surface and the adsorbed reactant (NH_4^+), which consumes part of the photo-generated charges, lowering their recombination. Consequently, the ammonia photodecomposition is expected to take place over the FeTiR sample. No significant PL signals were obtained for Fe_2O_3 .

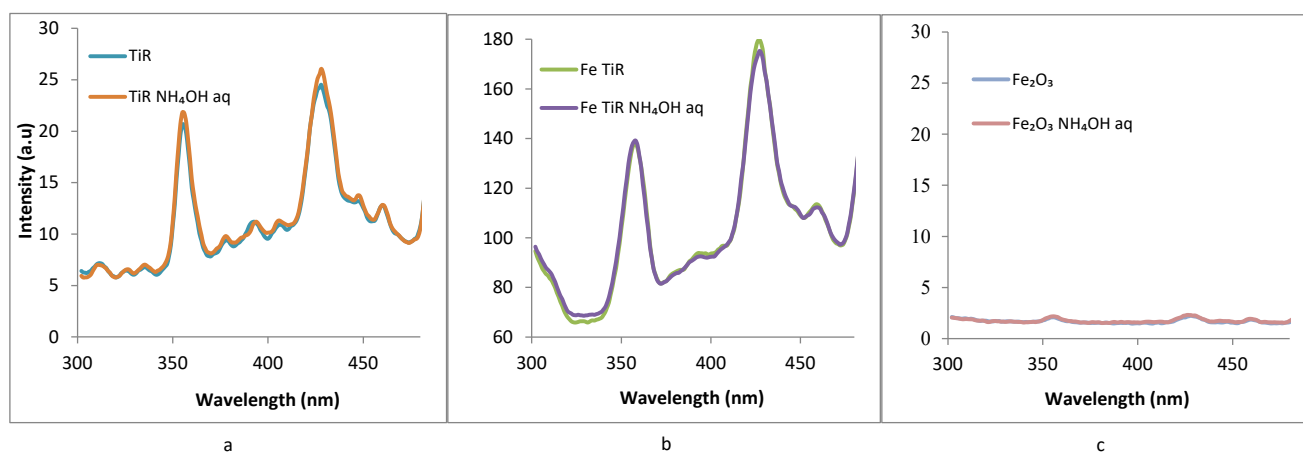


Figure 4. Room-temperature photoluminescence spectra of the powders suspended in water and diluted ammonia solutions, collected for $\lambda_{exc} = 260$ nm: (a) TiR, (b) FeTiR, (c) Fe_2O_3 .

2.2.5. Reactive Oxygen Species Generation: Hydroxyl Radical ($\cdot\text{OH}$) and Superoxide Anion (O_2^-)

Hydroxyl Radical ($\cdot\text{OH}$)

According to our previously reported data [28], the generation of $\cdot\text{OH}$ radicals was evaluated, taking into account the presence of fluorescent coumarin derivative (namely umbelliferone), caused by its interaction with photo-generated $\cdot\text{OH}$ radicals over the investigated materials.

The characteristic broad peak is located around 470 nm and is depicted in Figure 5a,b. If ammonia photo-oxidation is mediated by $\cdot\text{OH}$ radicals, this is likely to be caused by both TiR and FeTiR samples since they generate this oxygen species.

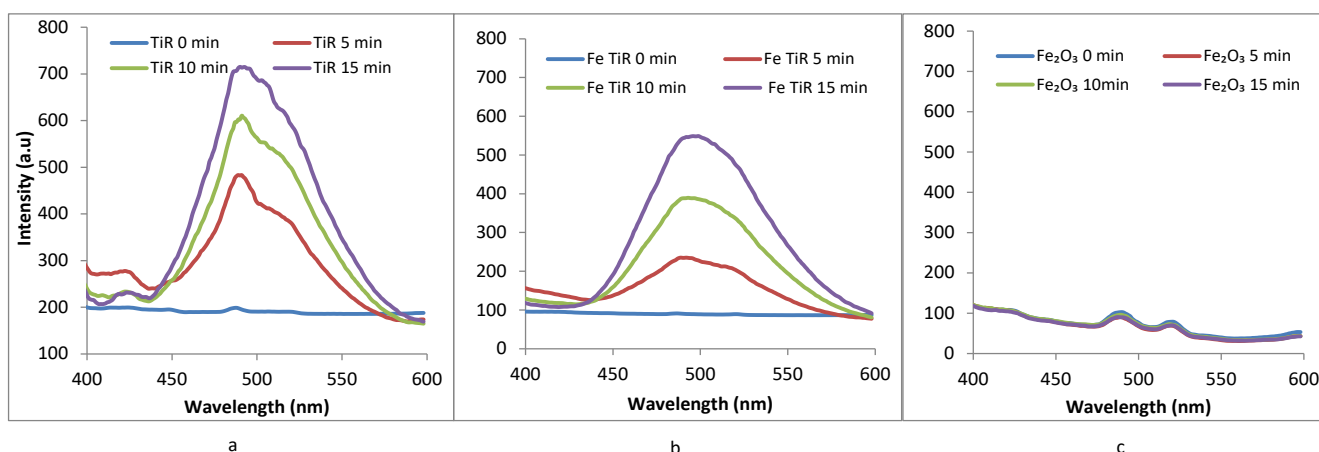


Figure 5. ·OH radicals trapping by coumarin under solar irradiation over TiR (a), FeTiR (b) and Fe₂O₃ (c).

Superoxide Anion (O₂[−])

In order to evaluate superoxide anion (O₂[−]) generation, the XTT Formazan complex formation (due to the reaction of XTT with the photogenerated O₂[−]) is evaluated based on spectrophotometric monitoring.

According to Figure 6a–c, there is no characteristic peak with maxima located at 475 nm for any of the investigated samples, only traces produced by Fe₂O₃ after 15 min of irradiation.

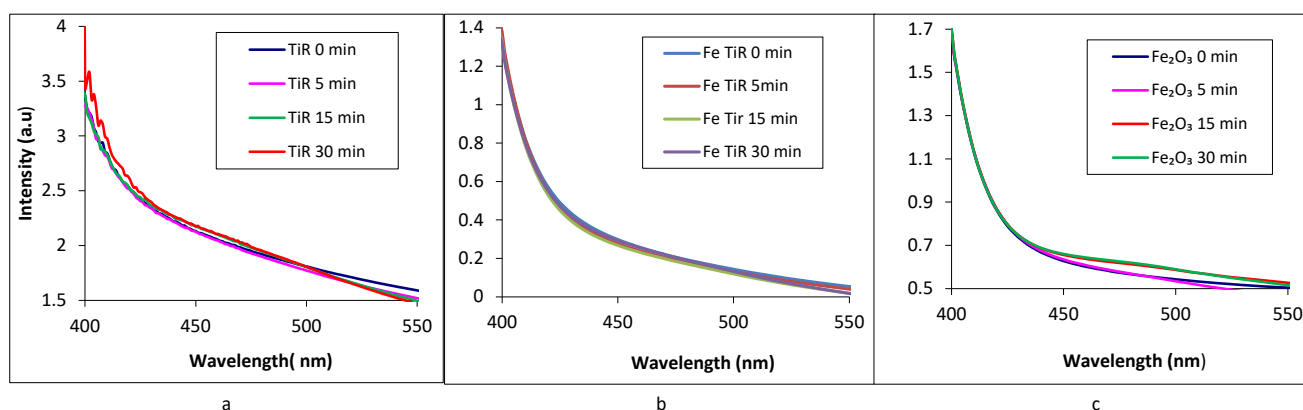


Figure 6. Investigation of O₂[−] generation over TiR (a), FeTiR (b), Fe₂O₃ cubes (c) under simulated solar light irradiation.

Consequently, it is reasonable to assume that the photogenerated electrons are not captured by O₂ but possibly involved in H₂ production.

2.2.6. Electrokinetic Potential Measurements

Electrokinetic potential measurements can reveal the surface properties of the interest powders suspended in water and diluted ammonia aqueous solution.

Figure 7 reveals the negative electrokinetic charges of all investigated samples. Nonetheless, a small difference in electrokinetic potential is observed for aqueous suspensions of titanate nanorods -49.54 mV and -45.24 for TiR and FeTiR, respectively. This could indicate more positive charges provided by the Fe presence in the titanate. Additionally, Fe₂O₃ cubes appear to be less negatively charged (electrokinetic potential being -29.2 mV). These above-mentioned values are clearly shifted toward the positive scale in the presence of ammonia. The difference is strongly related to the NH₄⁺ adsorption on the investigated

surfaces. These data confirm the electrostatically driven adsorption of NH_4^+ onto the catalyst surface for all samples.

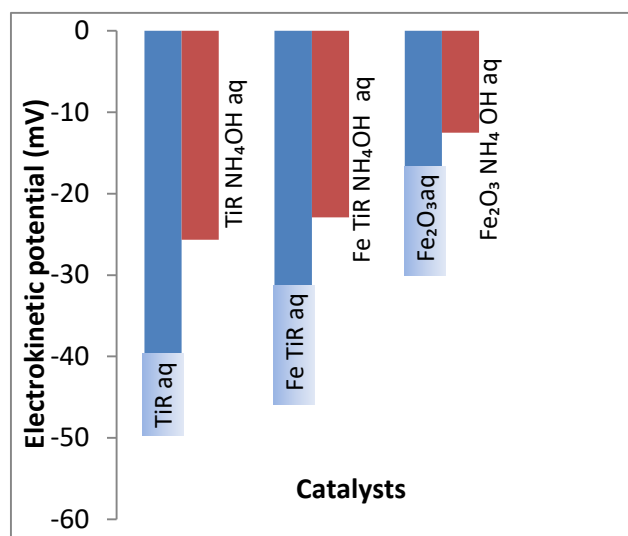


Figure 7. The electrokinetic potential of TiRs, Fe-modified TiRs and Fe₂O₃ cubes suspended in deionised water and diluted ammonia solution.

2.2.7. Photoelectrochemical Measurements

Current–potential dependence was registered for all samples under simulated solar light irradiation, before and after ammonia was added to the electrolyte.

The investigated powder suspensions were deposited by drop casting on transparent conductive oxide (TCO)-coated glass substrates. Figure 8 presents the plotted current density ($\mu\text{A}/\text{cm}^2$) versus potential (0–1 V) for the above-mentioned working electrodes under solar irradiation, before and after NH_4OH was added to the electrolyte solution. Lower values of the registered photocurrent density and open circuit voltage (V_{OC}) can be observed for the FeTiR relative to the TiR sample in both investigated media. Unlike the nanorods, the Fe₂O₃ cubes (green curve in Figure 8a) generate a much higher photocurrent that is significantly lowered by the ammonia addition.

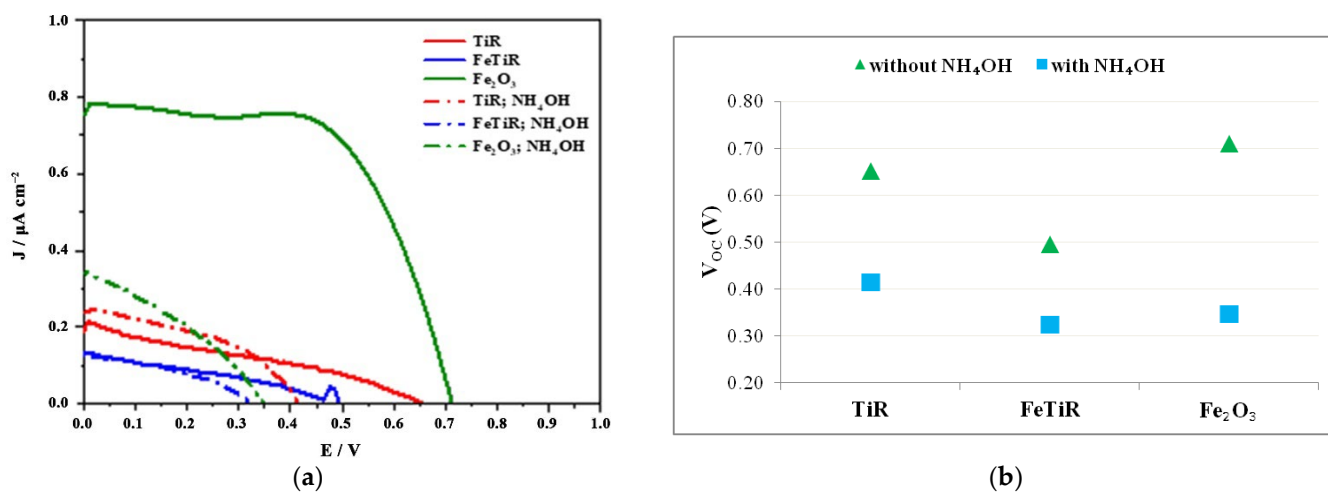


Figure 8. (a) J/V curves recorded for the investigated materials in pure electrolyte and diluted ammonia containing electrolyte under simulated solar irradiation; (b) V_{OC} representation for the investigated samples.

PCE (power conversion efficiency), η , was determined using the following equation:

$$\text{PCE} = \eta = \frac{J_{\text{sc}} V_{\text{oc}} \text{FF}}{P_{\text{in}}}$$

where: J_{sc} —short-circuit current density, V_{oc} —open-circuit voltage, FF—fill factor and P_{in} —power of incident light on the working electrode.

Figure 9 emphasizes the higher power conversion efficiency of the Fe_2O_3 sample in water that strongly decreases after the ammonia addition. On the contrary, the behaviour of the nanorods is scarcely affected by ammonia addition.

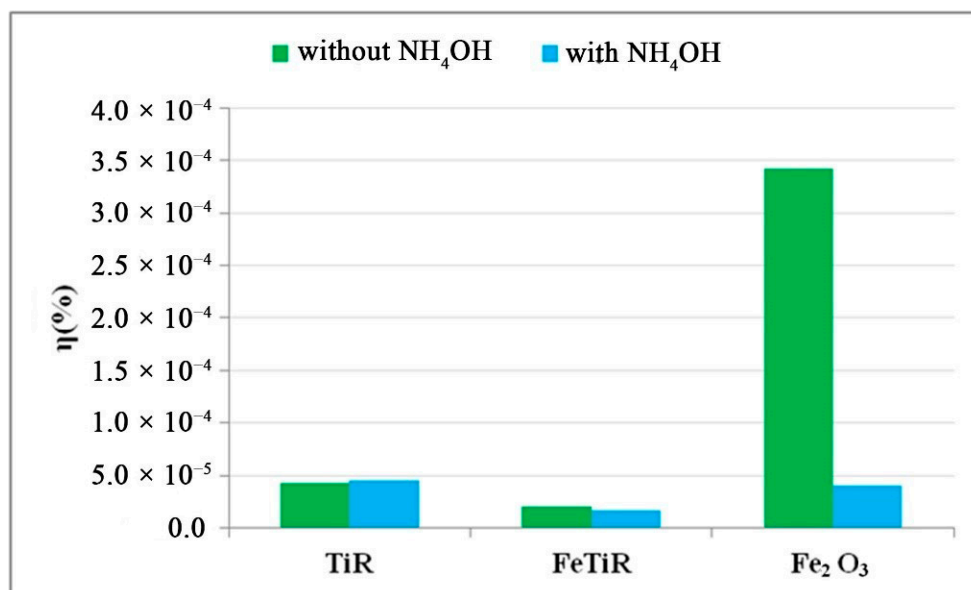


Figure 9. Comparative power conversion efficiency of the investigated samples measured in pure and ammonia containing electrolyte.

2.2.8. Temperature-Programmed Reduction Measurements (H_2 -TPR)

Hydrogen temperature-programmed reduction (H_2 -TPR) measurements were carried out to determine the redox behaviour of the involved chemical species of catalyst. As can be seen from Figure 10, the TiR sample is not significantly reduced in this temperature range. For the FeTiR and Fe_2O_3 samples, Figure 10 presents three similar but slightly shifted (to the higher temperature) peaks above 500°C . These correspond to the successive reduction stages of Fe_2O_3 to Fe^0 . The shift of the maxima to the higher temperatures in the case of Fe-modified nanorods could be due to the different encountering of the Fe species in titanate and Fe_2O_3 network, respectively. Unlike the Fe-modified nanorods, Fe_2O_3 cubes generate a distinct (TPR) peak around 450°C , which the previous literature assigns to the presence of iron hydroxide [29]. The next overlapped peaks from 500 to 600°C can be ascribed to the process of $\text{Fe}_2\text{O}_3 \rightarrow \text{Fe}_3\text{O}_4$. The largest hydrogen consumption at a high temperature 600 – 800°C can be assigned to the reduction of Fe_3O_4 to metallic iron via wüstite (FeO) $\text{Fe}_3\text{O}_4 \rightarrow \text{Fe}^0$ [30].

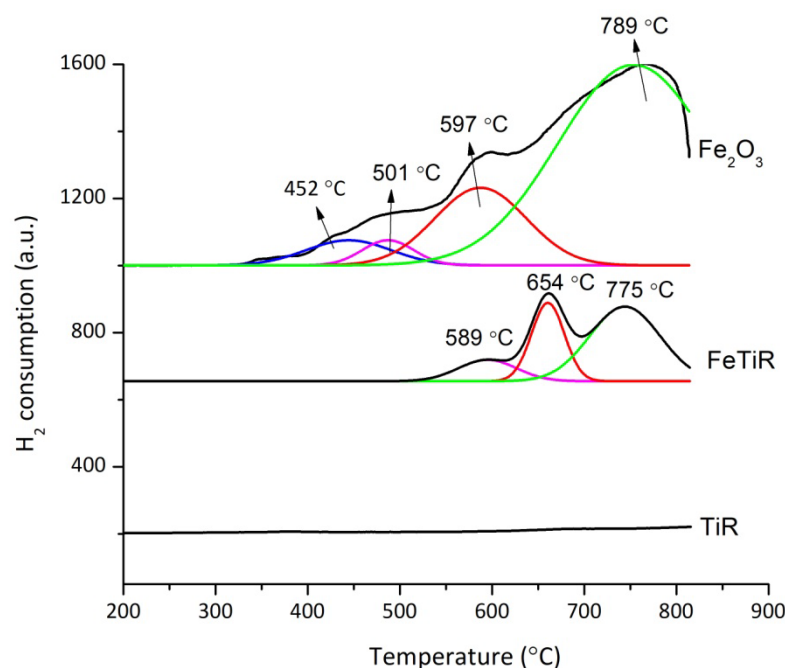


Figure 10. Temperature-programmed reduction behaviour of the investigated samples.

The amount of H₂ (μmol) consumed by each catalyst is listed in Table 2. It is clear that TiR sample is not significantly reduced in this temperature range.

Table 2. The H₂-TPR results for TiR, FeTiR and Fe₂O₃ catalysts.

Catalyst	H ₂ Consumption TPR (μmol/g)				Total H ₂ Consumption (μmol/g)
	I FeO(OH)	II Fe ₂ O ₃ → Fe ₃ O ₄	III Fe ^{2+,3+} → Fe ⁰	IV	
TiR	0	0	0	0	
FeTiR	0	128	244	232	604
Fe ₂ O ₃	1625	3092	4098	9352	18,167

In conclusion, in the FeTiR and Fe₂O₃ samples, the presence of Fe³⁺ as a single species can be identified using the TPR analysis. In the case of the Fe₂O₃ sample, besides hematite, the additional presence of an amorphous hydroxide phase is suggested. In fact, the XRD analysis indicates the presence of an amorphous phase (5%) for the Fe₂O₃ sample. The theoretical amount of H₂ consumption needed for the complete reduction of Fe³⁺ → Fe⁰ in pure Fe₂O₃ hematite is 18,750 μmol·g_{cat}⁻¹. The measured value was 18,167 μmol·g_{cat}⁻¹, which is close to the theoretical value. Concerning the synthesis procedure, the amorphous phase presence can be explained as follows. Despite the fact that the hydrothermal treatment applied for the obtaining of Fe₂O₃ cubes and FeTiR is similar, there is a significant difference regarding the overall synthesis procedure. The iron source of Fe₂O₃ nanocubes sample, obtained by hydrothermal synthesis, was FeCl₃·6H₂O in the aqueous solution. The sodium titanate nanorods were first subjected to an ion-exchange procedure in the presence of FeCl₃·6H₂O and were then hydrothermally treated.

2.2.9. Temperature-Programmed Desorption Measurements (NH₃-TPD)

The total acidity and distribution of the catalyst acid sites were calculated from the peak integration.

NH₃-TPD were performed in order to study the surface acidity of the FeTiR catalyst by comparing with TiR and Fe₂O₃. According to Figure 11 and Table 3, NH₃-TPD profiles of FeTiR, TiR and Fe₂O₃ catalysts were mainly composed of three desorption zones at the

following temperatures: 50–300 °C (weak acid groups), 300–600 °C (moderate acid sites) and 600–800 °C (strong acid sites), respectively.

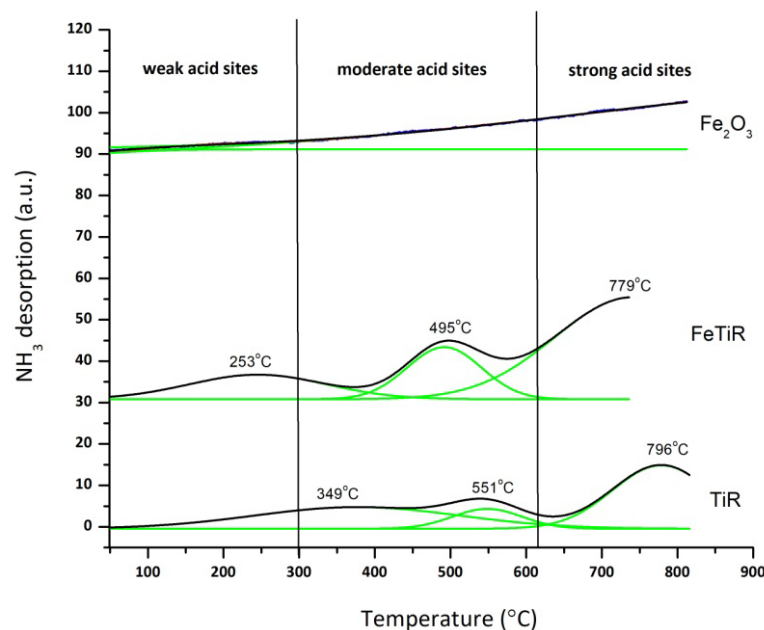


Figure 11. NH_3 -TPD profile.

Table 3. The total acidity and distribution of the acid sites of the TiR, Fe_2O_3 and FeTiR catalysts.

Catalysts	Weak Acid Sites	Moderate Acid Sites	Strong Acid Sites	Total Acid Sites
	$\mu\text{mol}\cdot\text{g}^{-1}$ $T < 300\text{ }^\circ\text{C}$	$\mu\text{mol}\cdot\text{g}^{-1}$ $300\text{ }^\circ\text{C} < T < 600\text{ }^\circ\text{C}$	$\mu\text{mol}\cdot\text{g}^{-1}$ $T > 600\text{ }^\circ\text{C}$	
TiR	0.185	0.682	9.764	10.631
FeTiR	0.714	2.204	11.989	14.907
Fe_2O_3	0.329	0.964	1.306	2.599

The thermal stability of the nanorods reached up to 350 °C, and the comparative evaluation of all investigated sample was perfectly valid for this temperature, which was similar to the structure of catalysts in our catalytic media. High-temperature investigations are relevant for comparisons with the literature data.

The total acidity of TiR sample increases after iron addition (FeTiR), while Fe_2O_3 does not absorb ammonia. Additionally, a shift of low-temperature desorption (from 349 to 253 °C) is observed after the Fe addition to TiR, indicating change in the surface acidity of the FeTiR catalyst. Wang et al. [31] showed that the NH_3 species adsorbed at a low temperature $T < 500\text{ }^\circ\text{C}$ can be related to the presence of Brønsted acid sites, while adsorption at a high temperature ($>600\text{ }^\circ\text{C}$) was correlated with the adsorption of NH_3 species on Lewis acid sites.

3. Catalytic Assays

Prior to ozone exposure and light irradiation, the steady state of the catalytical system is achieved (the suspended catalyst powder in aqueous ammonia solution is stirred for 30 min). It is expected that the reactant adsorption on the catalyst surface (certified by the electrokinetic potential measurements) and the working pH of the diluted ammonia solution are around 10. For these parameters, equilibrium occurs between free ammonia (NH_3) and ammonium ions (NH_4^+).

3.1. Ammonia Oxidation with Ozone

The following steps are presumably involved in aqueous ammonia catalytic oxidation with ozone:

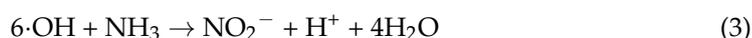
- An equilibrium reaction (Equation (1)):



- Direct oxidation with ozone, especially for low pH ($\text{pH} < \text{pKa}$):



- The reaction of $\cdot\text{OH}$ radicals resulting from the decomposition of O_3 (Equation (3)) ($\text{pH} > \text{pKa}$):



In both cases (Equations (4) and (5)), the oxidation of NO_2^- to NO_3^- occurs rapidly due to the strong oxidizing agents.

Figures 12 and 13 present the recorded catalytic results for the following working parameters: NH_4^+ initial concentration: 20.00 ppm, starting pH: 10.2, catalyst amount: 0.15 g/L, reaction temperature: 25 °C, and reaction time: 3 h.

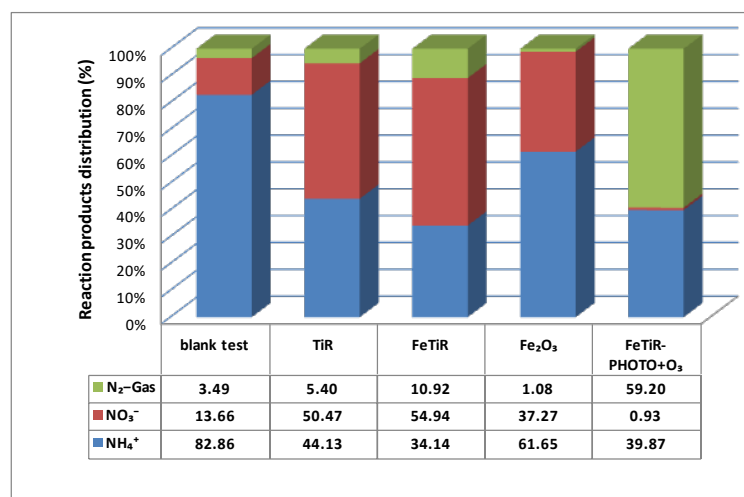


Figure 12. Reaction products distribution for aqueous ammonia oxidation with ozone and a photo-assisted process (carried out for FeTiR catalysts).

The amount of converted NH_4^+ in the absence of the catalyst (denoted as blank test in Figure 13) is low; a higher NH_4^+ conversion for the catalytic oxidation of ammonia with ozone is recorded over the FeTiR catalyst. The main degradation product in the solution is nitrate, and the nitrite ions are not present. A rapid oxidation of NO_2^- to NO_3^- in the presence of ozone occurs.

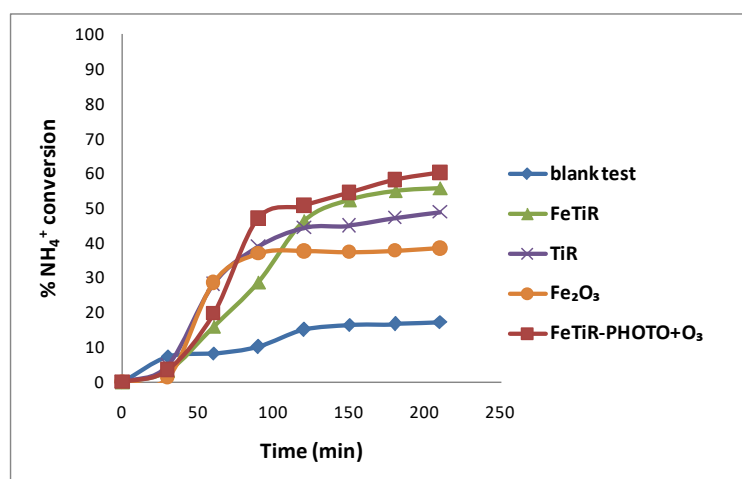


Figure 13. NH_4^+ conversion for catalytic oxidation with ozone and combined photo-assisted degradation pathway (for FeTiR catalyst).

Taking these data into account, the FeTiR sample was tested in a combined degradation pathway: ozone and solar light irradiation. An increase in conversion was recorded (Figure 13), together with a lower amount of NO_3^- . Based on these results, the increased selectivity of ammonia degradation to gaseous-nitrogen-containing end products is expected.

3.2. Photocatalytic Assays

The above-mentioned working parameters were preserved for the photocatalytic tests of the TiR, FeTiR, Fe_2O_3 samples. Similarly, the comparative evaluation of the combined photocatalytic ammonia oxidation with ozone was performed on the FeTiR sample and is presented in Figures 14 and 15.

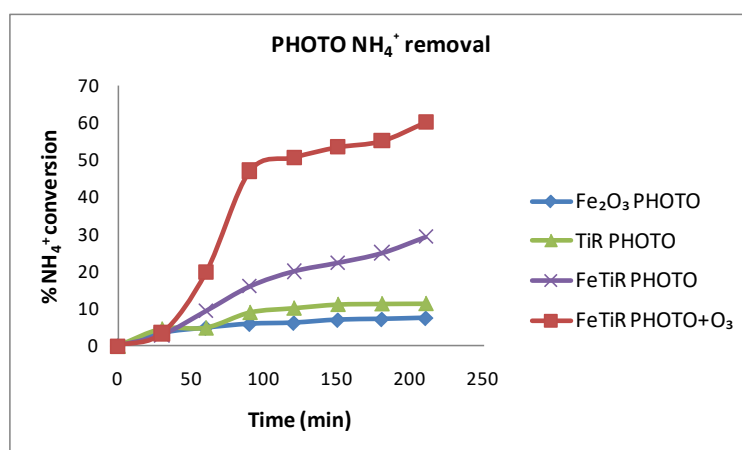
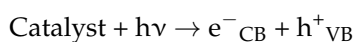


Figure 14. Comparative NH_4^+ photodegradation for the investigated samples.

After solar light irradiation of the system, the following steps are taken:



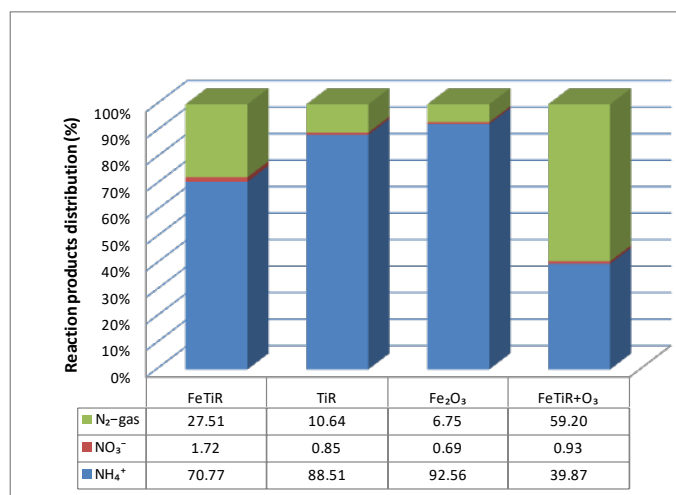


Figure 15. Reaction products distribution for aqueous ammonia photo-oxidation and ozone photo-assisted process (carried out for FeTiR catalyst).

According to the reported data [32], in the presence of oxygen, the following reactions are possible:

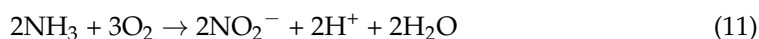


Figure 14 shows the highest NH₄⁺ conversion over the course of 180 min under solar irradiation and bubbled O₂ for the Fe-modified nanorods. The selectivity to gaseous nitrogen compounds is high (Figure 15) since the measured NO₃⁻ amount is very low and nitrite is also missing. By adding ozone to the photocatalytic system, an increased catalytic activity of this sample can be obtained. Figure 15 also emphasizes the improvement of NH₄⁺ conversion induced by ozone, adding to the photo-driven degradative process and reducing NO₃⁻ formation (1.72–0.93%).

Figure 16 shows the nitrate yield versus time of the ozonation process and photo-oxidation process. Due to the fact that the gaseous reaction products cannot be separately quantified, the yield of NO₃⁻ formation was measured. The lowest value was registered for the ozone photo-assisted degradation of ammonia for the FeTiR sample.

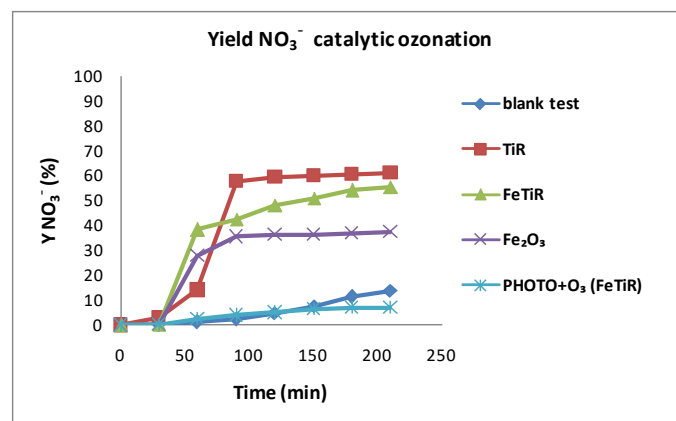


Figure 16. Yield of NO₃⁻ vs. time for ammonia ozonation in addition to photo-oxidation.

Taking into account the previously mentioned structural and functional characterization of the investigated catalysts, the following can be concluded for the photodegradative oxidation of the ammonia:

- The investigated ROS (both hydroxyl radicals and superoxide anions) are not fully involved in the degradative pathway.
- The photogenerated charges on the catalyst surface play a major role in ammonia oxidation.
- The highest photocatalytic activity of the Fe-modified titanate nanorods can be related to the increased light absorption relative to the bare samples.

4. Materials and Methods

4.1. Synthesis of Materials

The sodium titanate nanorods (TiR), Fe-modified titanate nanorods (FeTiR) and Fe₂O₃ were prepared, starting from commercial TiO₂, anatase (Aldrich), FeCl₃·6H₂O (Fluka), NaOH 97% (Alpha Aesar), and HCl 37.5% (Alfa Aesar).

4.2. Structural and Functional Characterization of the Obtained Materials

4.2.1. SEM—Scanning Electron Microscopy

In order to identify the morphological properties of the materials of interest, scanning electron microscopy (SEM) was used with a high-resolution microscope, FEI Quanta3 DFE model, Brno, Czech Republic, working at 5 kV voltage, in high-vacuum mode with Everhart–Thornley secondary electron (SE) detector, coupled with energy-dispersive X-ray (EDAX) spectrometer.

4.2.2. X-ray Diffraction (XRD) and X-ray Fluorescence (XRF)

Elemental analysis of the samples was carried out using a Rigaku ZSX Primus II spectrometer, Rigaku Corp., Tokyo, Japan with wavelength dispersion in vacuum atmosphere. The spectrometer was equipped with 4.0 kW X-ray Rh tube. The XRF results were analysed using EZ-scan combined with Rigaku SQX fundamental parameters software (standard less), which is capable of automatically correcting all matrix effects, including line overlaps.

Powder X-ray diffraction patterns were recorded using Rigaku's Ultima IV multi-purpose diffraction system, Rigaku Corp., Tokyo, Japan, a Cu target tube ($\lambda = 1.54060 \text{ \AA}$) and a graphite (002) monochromator, with working conditions of 30 mA and 40 kV. The data were collected at room temperature between 3 and 75° in 2 θ , with a 0.02° step size and a scanning rate of 1°/min. Phase identification was performed using Rigaku's PDXL software, connected to the ICDD PDF-2 database. The lattice constants were refined using diffraction line position.

4.2.3. UV–Vis Spectrophotometry

In order to investigate the optical properties of the investigated samples, the diffuse reflectance (DR) spectra were recorded with a UV–Vis spectrophotometer, Analytik Jena Specord 200 Plus, Jena, Germany. The diffuse reflectance UV–Vis data were converted into absorbance using the Kubelka–Munk function.

4.2.4. Photoluminescence (PL) Measurements

Photoluminescence (PL) data were obtained using a Carry Eclipse fluorescence spectrometer, Agilent Technologies, Kuala Lumpur, Malaysia, for the following working parameters: 120 nm min^{−1} scan rate, 0.5 nm spectral resolution, and 10 nm slits in excitation and emission. Powder samples (0.001 g) were suspended in ultrapure water. The measurements were performed at room temperature for $\lambda_{\text{exc}} = 260 \text{ nm}$.

4.2.5. Identification of Reactive Oxygen Species (ROS) Generation under Solar Irradiation

For ·OH radicals trapping, 1 mg of each catalyst was suspended in 10 mM coumarin (Merck) solution and exposed to simulated solar light irradiation for fluorescent umbel-

liferone formation. This was conducted with Carry Eclipse fluorescence spectrometer for $\lambda_{\text{exc}} = 330 \text{ nm}$.

For O_2^- formation, 3 mg of each sample was suspended in 3 mM solution of XTT sodium salt (2, 3-bis(2-methoxy-4-nitro-5-sulfophenyl)-2H-tetrazolium-5-carboxanilide) (Sigma-Aldrich) and exposed to simulated solar light, following XTT reduction by the photogenerated O_2^- . These results in the formation of XTT formazan complex were identified with a UV-Vis spectrophotometer, Analytik Jena Specord 200 Plus, a broad peak located at 470 nm being indicative.

4.2.6. Electrokinetic Potential Measurements

Electrokinetic potential measurements were carried out on a Malvern Nano ZS Zetasizer, Model ZEN 3600, Malvern, UK, at room temperature. The electrokinetic potential values were calculated using Helmholtz–Smoluchowski equation. The tests were conducted in triplicate.

4.2.7. Photoelectrochemical (PEC) Tests

Photoelectrochemical measurements were carried out in an electrochemical cell equipped with a quartz window using a two-electrode configuration by means of a Zahner IM6 potentiostat, Zahner-Elektrik GmbH, Kronach—Gundelsdorf, Germany. The reference and counter electrode leads were connected to a platinum wire, and working electrode lead was attached to prepared samples (geometric area of $\sim 3 \text{ cm}^2$). An aqueous suspension of interest powder (0.01 g in 2 mL ultrapure water) was sonicated and coated on TCO conductive glass (Solaronix, Aubonne, Switzerland) by successive depositions and subsequent drying. The as-obtained coatings were heat treated at $300 \text{ }^\circ\text{C}$ in air for 1 h. The experiments were conducted in 0.5 M Na_2SO_4 electrolyte, pure or containing NH_4OH (12 $\mu\text{L}/120 \text{ mL}$) under simulated solar light irradiation (AM 1.5, Peccell-L01, Yokohama, Japan). Photocurrent–voltage curves were recorded by linear sweep voltammetry at a scan rate of 10 mV/s.

4.2.8. H_2 -TPR-Hydrogen Temperature-Programmed Reduction

Hydrogen temperature-programmed reduction (H_2 -TPR) was carried out to determine the reducibility of catalytic species using the CHEMBET 3000 Quantachrome apparatus, Boynton Beach, FL, USA. The sample (20 mg) was heated from room temperature up to 1073 K with 10 K/min heating rate, using a stream of 5% H_2/Ar . The hydrogen consumption was estimated from the area of the recorded peaks.

The calibration of the TCD signal was performed by injecting a known quantity of hydrogen (typically 50 μL) in the carrier gas (Ar). The experimentally obtained peak surface ($\text{mV}\cdot\text{s}$) was thus converted into micromoles of hydrogen.

4.2.9. NH_3 -TPD Temperature-Programmed Desorption

Quantity and distribution of acid sites were performed by temperature-programmed desorption of ammonia (NH_3 -TPD) technique with the same apparatus mentioned above. Before the measurement, the catalyst was saturated using 200 μL injected pulse NH_3 gas at $50 \text{ }^\circ\text{C}$. The NH_3 -TPD experiment was carried out in a flow system with thermal conductivity detectors (TCD) by heating with 10 K/min (from room temperature up to 1073 K). This was used as a carrier gas ($70 \text{ mL}\cdot\text{min}^{-1}$). The NH_3 desorption was estimated from the area of the recorded peaks. The calibration of the TCD signal was performed by injecting a known quantity of NH_3 . The surface of the as-obtained peak ($\text{mV}\cdot\text{s}$) was converted into micromoles of ammonia.

4.3. Catalytic Ozonation and Photocatalytic Tests

Ozonation of ammonia in water was performed by using a semi-batch reactor connected to a gas flow line. Aside from the reactor, the catalytic setup contained a pH meter, stirring system, and a recirculator to maintain a constant temperature ($25 \text{ }^\circ\text{C}$) and an ozone-generating source. Typically, 0.015 g of catalyst was added into 100 mL of the ammonia

solution containing 20 ppm NH_4^+ . The suspension was vigorously stirred in a stream of O_3/O_2 ($10 \text{ cm}^3 \cdot \text{min}^{-1}$). O_3 was generated from O_2 using an ozone generator (OzoneFIX, Mureş, Romania).

Photocatalytic tests of aqueous ammonia oxidation were carried out in a photoreactor (120 mL) provided with a quartz window and thermostated at 18°C . Catalyst (0.015 g) was suspended in ammonia solution containing 20 ppm NH_4^+ obtained by adding of ammonia solution (NH_4OH 25%) in ultrapure water. Light irradiation of the reaction medium (AM 1.5) was realised by exposing it to AM 1.5 light provided by a solar simulator (PecceLL-L01) with a xenon short-arc lamp (150 W). A gaseous mixture of argon ($10 \text{ cm}^3 \cdot \text{min}^{-1}$) and oxygen ($1 \text{ cm}^3 \cdot \text{min}^{-1}$) was bubbled into the aqueous suspension. The liquid aliquots were collected every 30 min and analysed with ion chromatographs (Dionex ICS 900, Sunnyvale, CA, USA) for the monitoring of NH_4^+ and the resulting anions (NO_3^-).

Ammonia oxidation with ozone, assisted by solar light irradiation, was performed using the above-mentioned set-up, also equipped with an ozone generator:

$$X_{\text{NH}_4^+} \% = \frac{[\text{NH}_4^+]_t}{[\text{NH}_4^+]_i} * 100 \quad (13)$$

$$S_{\text{N}_2 - \text{gas}} \% = 100 - S_{\text{NO}_3^-} \% \quad (14)$$

$$S_{\text{NO}_3^-} \% = \frac{[\text{NO}_3^-]_t}{[\text{NH}_4^+]_c} * 100 \quad (15)$$

$$Y_{\text{NO}_3^-} \% = \frac{[\text{NO}_3^-]_t}{[\text{NH}_4^+]_i} * 100 \quad (16)$$

where: $X_{\text{NH}_4^+}$ is the NH_4^+ conversion, $Y_{\text{NO}_3^-}$ is the yield of NO_3^- , $[\text{NH}_4^+]_t$ is the ammonium ion concentration consumed at time t , $[\text{NH}_4^+]_i$ is initial ammonium ion concentration, and $[\text{NO}_3^-]_t$ is the nitrate concentration formed at time t .

5. Conclusions

Hydrothermally synthesized titanate nanorods were successfully modified by the addition of Fe precursor.

$\alpha\text{-Fe}_2\text{O}_3$ with a well-defined morphology (nanocubes) was obtained by similar hydrothermal treatment and tested for comparative evaluation.

The comparison of the structural and functional characterization data of both titanate-based samples showed that the modification of titanate nanorods with iron did not affect the nanorod morphology and significantly improved optical and photocatalytic properties.

Catalytic investigations for aqueous ammonia oxidation showed the best reactivity for the Fe-modified sample (FeTiR) under solar light irradiation and ozonation. The NH_4^+ conversion and selectivity to gaseous end products was further improved by combining ozonation with the photo-assisted catalytic oxidation of aqueous ammonia.

An environmentally friendly, non-expensive and innovative depollution technology can be developed based on these materials.

Author Contributions: Conceptualization, S.P., M.Z., C.A. and F.P.; methodology, C.A., I.B. and F.P.; formal analysis, investigation, S.P., P.U., C.A., F.P., S.V.P., C.G. and R.S.; data curation, D.-I.E. I.B. and C.A.; writing—original draft preparation, C.A., F.P., S.V.P. and R.S.; writing—review and editing, C.A., R.S. and F.P.; supervision, I.B.; funding acquisition, C.A. and F.P. All authors have read and agreed to the published version of the manuscript.

Funding: This research was funded by Unitatea Executiva pentru Finantarea Invatamantului Superior, a Cercetarii, Dezvoltarii si Inovarii (UEFISCDI), grant number: PN-III-P2-2.1-PTE-2019-0222, 26PTE/2020 DENOX.

Conflicts of Interest: The authors declare no conflict of interest.

References

1. Oller, I.; Malato, S.; Sánchez-Pérez, J.A. Combination of Advanced Oxidation Processes and biological treatments for wastewater decontamination—A review. *Sci. Total Environ.* **2011**, *409*, 4141–4166. [[CrossRef](#)] [[PubMed](#)]
2. Shiskowski, D.M.; Mavinic, D.S. Biological treatment of a high ammonia leachate: Influence of external carbon during initial startup. *Water Res.* **1998**, *32*, 2533–2541. [[CrossRef](#)]
3. Malone, R.F.; Pfeiffer, T.J. Rating fixed film nitrifying biofilters used in recirculating aquaculture systems. *Aquacult. Eng.* **2006**, *34*, 389–402. [[CrossRef](#)]
4. Yuan, M.-H.; Chen, Y.-H.; Tsai, J.-Y.; Chang, C.-Y. Removal of ammonia from wastewater by air stripping process in laboratory and pilot scales using a rotating packed bed at ambient temperature. *J. Taiwan Inst. Chem. Eng.* **2016**, *60*, 488–495. [[CrossRef](#)]
5. Devi, P.; Dalai, A.K. Implications of breakpoint chlorination on chloramines decay and disinfection by-products formation in brine solution. *Desalination* **2021**, *504*, 114961. [[CrossRef](#)]
6. Bhuiyan, M.I.H.; Mavinic, D.; Beckie, R. Nucleation and growth kinetics of struvite in a fluidized bed reactor. *J. Cryst. Growth* **2008**, *310*, 1187–1194. [[CrossRef](#)]
7. Pansini, M. Natural zeolites as cation exchangers for environmental protection. *Miner. Depos.* **1996**, *31*, 563–575. [[CrossRef](#)]
8. Ichikawa, S.I.; Mahardiani, L.; Kamiya, Y. Catalytic oxidation of ammonium ion in water with ozone over metal oxide catalysts. *Catal. Today* **2014**, *232*, 192–197. [[CrossRef](#)]
9. Krisbiantoro, P.A.; Togawa, T.; Kato, K.; Zhang, J.; Otomo, R.; Kamiya, Y. Ceria-supported palladium as a highly active and selective catalyst for oxidative decomposition of ammonium ion in water with ozone. *Catal. Commun.* **2021**, *149*, 106204. [[CrossRef](#)]
10. Chen, Y.; Wu, Y.; Liu, C.; Guo, L.; Nie, J.; Chen, Y.; Qiu, T. Low-temperature conversion of ammonia to nitrogen in water 2 with ozone over composite metal oxide catalyst. *J. Environ. Sci.* **2018**, *66*, 265–273. [[CrossRef](#)]
11. Taguchi, J.; Okuhara, T. Selective oxidative decomposition of ammonia in neutral water to nitrogen over titania-supported platinum or palladium catalyst. *Appl. Catal. A Gen.* **2000**, *194*, 89–97. [[CrossRef](#)]
12. Ukropec, R.; Kuster, B.F.M.; Schouten, J.C.; van Santen, R.A. Low temperature oxidation of ammonia to nitrogen in liquid phase. *Appl. Catal. B Environ.* **1999**, *23*, 45–47. [[CrossRef](#)]
13. Wang, Y.; Xu, W.; Li, C.; Yang, Y.; Geng, Z.; Zhu, T. Effects of IrO₂ nanoparticle sizes on Ir/Al₂O₃ catalysts for the selective oxidation of ammonia. *Chem. Eng. J.* **2022**, *437*, 135398. [[CrossRef](#)]
14. Dobrescu, G.; Papa, F.; State, R.; Balint, I. Characterization of bimetallic nanoparticles by fractal analysis. *Powder Technol.* **2018**, *338*, 905–914. [[CrossRef](#)]
15. State, R.; Papa, F.; Dobrescu, G.; Munteanu, C.; Atkinson, I.; Balint, I.; Volceanov, A. Green synthesis and characterization of gold nanoparticles obtained by a direct reduction method and their fractal dimension. *Environ. Eng. Manag. J.* **2015**, *14*, 587–593. [[CrossRef](#)]
16. Shavisi, Y.; Sharifnia, S.; Mohamadi, Z. Solar-Light-Harvesting Degradation of Aqueous Ammonia by CuO/ZnO Immobilized on Pottery Plate: Linear Kinetic Modeling for Adsorption and Photocatalysis Process. *J. Environ. Chem. Eng.* **2016**, *4*, 2736–2744. [[CrossRef](#)]
17. Bahadori, E.; Conte, F.; Tripodi, A.; Ramis, G.; Rossetti, I. Photocatalytic Selective Oxidation of Ammonia in a Semi-Batch Reactor: Unravelling the Effect of Reaction Conditions and Metal Co-Catalysts. *Catalysts* **2021**, *11*, 209. [[CrossRef](#)]
18. Wang, I.; Edwards, J.G.; Davies, J.A. Photooxidation of aqueous ammonia with titania-based heterogeneous catalysts. *Sol. Energy* **1994**, *52*, 459–466. [[CrossRef](#)]
19. Bavykin, D.V.; Friedrich, J.M.; Walsh, F.C. Protonated Titanates and TiO₂ Nanostructured Materials: Synthesis, Properties and Applications. *Adv. Mater.* **2006**, *18*, 2807–2824. [[CrossRef](#)]
20. Amy, L.; Favre, S.; Gau, D.L.; Faccio, R. The effect of morphology on the optical and electrical properties of sodium titanate nanostructures. *Appl. Surf. Sci.* **2021**, *555*, 149610. [[CrossRef](#)]
21. Sayahi, H.; Aghappor, K.; Mohsenzadeh, F.; Morad, M.M.; Darabi, H.R. TiO₂ nanorods integrated with titania nanoparticles: Large specific surface area 1D nanostructures for improved efficiency of dye-sensitized solar cells (DSSCs). *Sol. Energy* **2021**, *215*, 311–320. [[CrossRef](#)]
22. Kerkez, O.; Boz, I. Photo(electro)catalytic Activity of Cu²⁺-Modified TiO₂ Nanorod, Array Thin Films under Visible Light Irradiation. *J. Phys. Chem. Solids* **2014**, *75*, 611–618. [[CrossRef](#)]
23. Preda, S.; Anastasescu, C.; Balint, I.; Umek, P.; Sluban, M.; Negrila, C.; Angelescu, D.G.; Bratan, V.; Rusu, A.; Zaharescu, M. Charge separation and ROS generation on tubular sodium titanates exposed to simulated solar light. *Appl. Surf. Sci.* **2019**, *470*, 1053–1063. [[CrossRef](#)]
24. Ma, J.; Lian, J.; Duan, X.; Liu, X.; Zheng, W. α -Fe₂O₃: Hydrothermal Synthesis, Magnetic and Electrochemical Properties. *J. Phys. Chem. C* **2010**, *114*, 10671–10676. [[CrossRef](#)]
25. Andrusenko, I.; Mugnaioli, E.; Gorelika, T.E.; Koll, D.; Panthöfer, M.; Tremelb, W.; Kolb, U. Structure analysis of titanate nanorods by automated electron diffraction tomography. *Acta Crystallogr. Sect. B Struct. Sci.* **2011**, *67*, 218–225. [[CrossRef](#)]
26. Shirpour, M.; Cabana, J.; Doef, M. New materials based on a layered sodium titanate for dual electrochemical Na and Li intercalation systems. *Energy Environ. Sci.* **2013**, *6*, 2538–2547. [[CrossRef](#)]

27. Liqiang, J.; Yichun, Q.; Baiqi, W.; Shudan, L.; Baojiang, J.; Libin, Y.; Wei, F.; Honggang, F.; Jiazhong, S. Review of photoluminescence performance of nano-sized semiconductor materials and its relationships with photocatalytic activity. *Sol. Energy Mater. Sol. Cells* **2006**, *90*, 1773–1787. [[CrossRef](#)]
28. Anastasescu, C.; Negri, C.; Angelescu, D.G.; Atkinson, I.; Anastasescu, M.; Spataru, N.; Zaharescu, M.; Balint, I. Distinct and interrelated facets bound to photocatalysis and ROS generation on insulators and semiconductors: Cases of SiO₂, TiO₂ and their composite SiO₂-TiO₂. *Catal. Sci. Technol.* **2018**, *8*, 5657–5668. [[CrossRef](#)]
29. Liu, B.; Geng, S.; Zheng, J.; Jia, X.; Jiang, F.; Liu, X. Unravelling the new roles of Na and Mn promoter in CO₂ hydrogenation over Fe₃O₄-Based catalysts for enhanced selectivity to light α -olefins. *ChemCatChem* **2018**, *10*, 4718–4732. [[CrossRef](#)]
30. Stoicescu, C.S.; Culita, D.; Stanica, N.; Papa, F.; State, R.N.; Munteanu, G. Temperature programmed reduction of a core-shell synthetic magnetite: Dependence on the heating rate of the reduction mechanism. *Termochim. Acta.* **2022**, *709*, 179146. [[CrossRef](#)]
31. Wang, X.; Zhao, Z.; Xu, Y.; Li, Q. Promoting effect of Ti addition on three-dimensionally ordered macroporous Mn-Ce catalysts for NH₃-SCR reaction: Enhanced N₂ selectivity and remarkable water resistance. *Appl. Surf. Sci.* **2021**, *569*, 151047. [[CrossRef](#)]
32. Shibuya, S.; Aoki, S.; Sekine, Y.; Mikami, I. Influence of oxygen addition on photocatalytic oxidation of aqueous ammonia over platinum-loaded TiO₂. *Appl. Catal. B Environ.* **2013**, *138–139*, 294–298. [[CrossRef](#)]